Characterization of solar over-irradiance events in Uruguay

Paola Russo[1], Agustín Laguarda[2] and Gonzalo Abal[1]

[1] Laboratorio de Energía Solar, CENUR LN, Salto (Uruguay)

[2] Laboratorio de Energía Solar, Facultad de Ingeniería, Montevideo (Uruguay)

Abstract

The first characterization of over-irradiance (OI) events in Uruguay is presented. These events are associated to high diffuse and global irradiance and occur during short time intervals for specific sky conditions. Their local characterization is of interest due to their potential impact on solar energy systems. A 1-minute solar irradiance time series with several years of data is used to identify and characterize OI events over one site representative of the broader Pampa Húmeda region. These events were observed in 4.1 % of the filtered data records and the maximum horizontal irradiance was 1601 W/m^2 (18% above the mean extraterrestrial irradiance). The duration, intensity and seasonality of OI events is analyzed.

Keywords: over-irradiance, solar resource assessment, solar radiation, clear-sky model

1. Introduction

Over-irradiance (OI) events are a short-term phenomenon characterized by a rapid increase of global horizontal irradiance (G) above the expected clear sky irradiance. These events can last several minutes and result in global irradiances larger than the irradiance at the top of the atmosphere (TOA). G values exceeding 1400 W/m2, 1650 W/m2, 1634 W/m2 or even 1691 W/m2 have been registered at the 1-minute timescale in different sites as reported by Inman (2016), de Andrade and Tiba (2016), Gueymard (2017) and Castillejos (2020). OI events are also known as cloud-enhancement events, because they occur under partially cloudy conditions and imply an enhancement of the diffuse component of global irradiance due to cloud reflection. However, OI events can also involve fluctuations in beam irradiance, as noted in Gueymard (2017).

The study of OI events is relevant for a proper characterization of the solar resource. For instance, OI events may affect the expected output of a PV power plant causing peaks in the generated power which are difficult to account by forecasting models, as mentioned by Castillejo-Cuberos (2020) and also Järvelä et al. (2020). In solar resource assessment, detecting OI events and treating them differently from the data samples coming from clear-sky conditions or cloudy conditions, can lead to better results in model performance (Gueymard, 2017). In data quality control, it is important to identify OI events, since some filters might mistakenly flag them as invalid samples, when the measured values are actually correct, as noted in Castillejo-Cuberos and Escobar (2020). OI events detection and characterization is also relevant for health risk prevention, in order to prevent the exposure to intense solar UV radiation and its associated negative impacts on human health. Finally,

the frequency and intensity of OI events is relevant in the design of materials which will be exposed to the sun for long time periods, in order to estimate their expected durability under real conditions.

This work presents a first characterization of OI events in a 5-year time series of global horizontal solar irradiance recorded at 1-minute intervals at the main measurement station of the Solar Energy Laboratory (LES http://les.edu.uy) located in Salto, Uruguay, a site that is representative of the broader Pampa Húmeda region. A simple methodology to detect OI events is used, which maximizes the accuracy of OI detections. The chosen methodology is based only on global solar irradiance measurements, so that it can be used later at other sites where only global horizontal irradiance data is available, to analyze the spatial distribution of OI events in the target territory. Several characteristics of the OI events are considered: duration, magnitude, peak intensity and temporal distribution.

2. Data and methodology

2.1 Data

The data used in this work consists of simultaneous records of global (G), direct (G_b) and diffuse horizontal (G_d) irradiance registered at 1-minute intervals at the Solar Energy Laboratory (LES) (latitude 31.27º W, longitude 57.89º S and altitude 56 m a.s.l.). The station is mounted on a Kipp & Zonen SOLYS 2 precision solar tracker fitted with a shading ball assembly and a sun sensor for fine adjustments. The global and diffuse irradiances are measured with class A spectrally flat pyranometers (under ISO 9080:2018 standard) and G_b is measured with a class A CHP1 pyrheliometer. All the instruments are periodically calibrated (every two years, at most) at the laboratory with traceability to the World Radiometric Reference maintained by PMOD/WRC at Davos. The instruments for global and diffuse irradiance are ventilated using standard Kipp & Zonen CV4 heaters/ventilators to avoid problems with dust or water droplets in the domes. These instruments are supervised and maintained at least on a weekly basis.

Table 1: Filtered samples by quality control procedure (QC) and solar altitude.. On the last column the cumulative percentage of discarded data from the initial set is shown in each step, as the % of selected clear sky data.

# diurnal samples	1311947	**% of diurnal samples**
# samples that pass QC.	962430	disc. 26.6 %
# diurnal samples with solar altitude > 7º	947015	total disc. 27.8 %
# clear sky samples	397622	selected 30.3 %

The data set corresponds to five years (2016-2020) of continuous monitoring and has been subjected to adequate quality control procedures based on BSRN recommendations by Mc. Arthur (2005), omitting the upper limits so as not to remove possible OI events. Only data with solar altitudes greater than 7º are considered for this analysis, to reduce the impact of

cosine errors. Some OI events with lower solar altitudes may exist but they are associated with low G values and are not the focus of this work. Table 1 shows the number of samples of the initial diurnal data set, and that of the subsets that pass the quality filter and solar height. The percentage of the initial sample discarded in each step is expressed in parentheses.

2.2 Methodology

An accurate detection of OI events is crucial for a proper characterization. Several methods can be used to define and detect OI events, three of which are used by Castillejos-Cuberos (2020). After testing several methods, in this work we identify OI events as those records for which the global irradiance (G) is above the current clear-sky estimate (G_{cs}) by a certain threshold,

$$G > G_{cs} \times (1 + \xi) \qquad\qquad (eq.\ 1)$$

where ξ is a positive dimensionless threshold to be determined. This criterion is simple, accurate and is based only on G measurements, so it's scalable to other sites. The determination of the optimum threshold ξ is discussed in detail in the next Subsection. eq. (1) is used in an algorithm for the automatic detection of OI samples in the 1-minute global irradiance time series. Once the set of over-irradiance samples has been determined, its statistics are calculated. The analysis considers the relevant characteristics of 1-minute OI samples but also of consecutive over-irradiance periods or OI events (OIE), as described in the following Subsection.

2.3 Over Irradiance detection

A clear-sky model is required for the identification of OIE from eq. (1). In this work, the ESRA clear-sky model (Rigollier 2000) is used. This model uses the Linke Turbidity (T_L) as its single atmospheric parameter and it can be accurate over the region of interest, when used with locally derived cycles of daily mean T_L, as studied in Laguarda and Abal (2017), Laguarda et al. (2020). Additional validation of the model, including the one done for this work, is described below. The model is based on average atmospheric information and in particular it is not sensitive to small intra-day variations in the atmosphere. However, it is simple and adequate for the purposes of OI sample detection.

Clear-sky model validation

The ESRA model (with local T_L cycles) has been validated over the region in (Laguarda et al., 2021) at the hourly timescale using clear-sky irradiance measurements from several sites, including the one considered in this work.

The metrics used in the validation are the usual relative Mean Bias Deviation (rMBD) and the relative Root Mean Square Deviation (rRMSD), both expressed as a % of the

measurement mean. Additionally, the Kolmogorov-Smirnov Integral (KSI), which measures the distance between the cumulative probability of the estimated and the reference series, is calculated. See Laguarda and Abal (2017) or Gueymard (2014) for detailed definitions and examples of their usage in the solar resource assessment context.

The hourly validation done in (Laguarda et al., 2021) for the site considered in this work was performed using a standard random sampling and cross-validation process and shows a negative rMBD of -0.2%, rRMSD of 2.9% and a KSI of 5.2 Wh/m². For this work, a new validation was done at the 1-minute timescale, with the results listed in Table 2 below. The clear sky samples were selected using the method described in Reno et al. (2016), imposing strict thresholds to avoid false positives. In order to remove a potential dependence of the OI characterization's results with the clear sky model chosen, a standard linear site adaptation, as described by Polo (2016), was applied to the raw ESRA estimates. This procedure results in an unbiased version with an rRMSD of 3.5% (see Table 2), which is similar to the instrument's uncertainty for 1-minute records. The site-adapted ESRA will be used from here on as the clear-sky model.

Tab.2: Performance of original and site adapted GHI estimates of ESRA clear sky model implemented for this work.

	original (%)	site adapted (%)
rMBD (%)	-3.8	0.0
rRMSD (%)	5.2	3.5
KSI (W/m²)	23.6	17.1
% relative to the average of 397622 clear sky measurements = 624.6 W/m²		

Determination of the threshold ξ

As stated in eq. (1), a global irradiance measurement is considered OI when it exceeds the site-adapted clear-sky model by a coefficient $1+\xi$ so a proper choice of the threshold ξ is essential for accurate results. Low values of ξ enhance the chance of incorrectly tagging clear sky samples as OI (false positives). On the other hand, high ξ values will select only a subset of the real OI events (false negatives). The optimum value for ξ must be determined from the data and visual inspection by a careful analysis.

The fraction of selected clear sky samples that *are not tagged as OI* is shown in Fig. 1, in terms of ξ. In order to balance this two effects, we impose $\xi = 0.105$, which equals 3 standard deviations (as estimated from the ESRA model uncertainty, i.e. P99 confidence level for a normal distribution of the residuals). Figure 1 shows that for $\xi = 0.105$ less than 1% of the detected clear sky samples are tagged as OI. This is a rather restrictive test as compared, for instance, with (Castillejos-Cuberos, 2020) which uses a 1.05 as a threshold

($\xi = 0.05$), but it reduces the chances of incorrect OI identification, as confirmed by visual inspection of several OI samples.

Selection of OI events

After an initial step with $\xi = 0.105$, a few clear-sky samples are still erroneously identified as OI events. Thus, in a second iteration, the few clear sky samples incorrectly selected as OI are removed using the clear sky detection algorithm provided by PVlib by Holmgren (2018) based on the criteria described in Reno (2016).
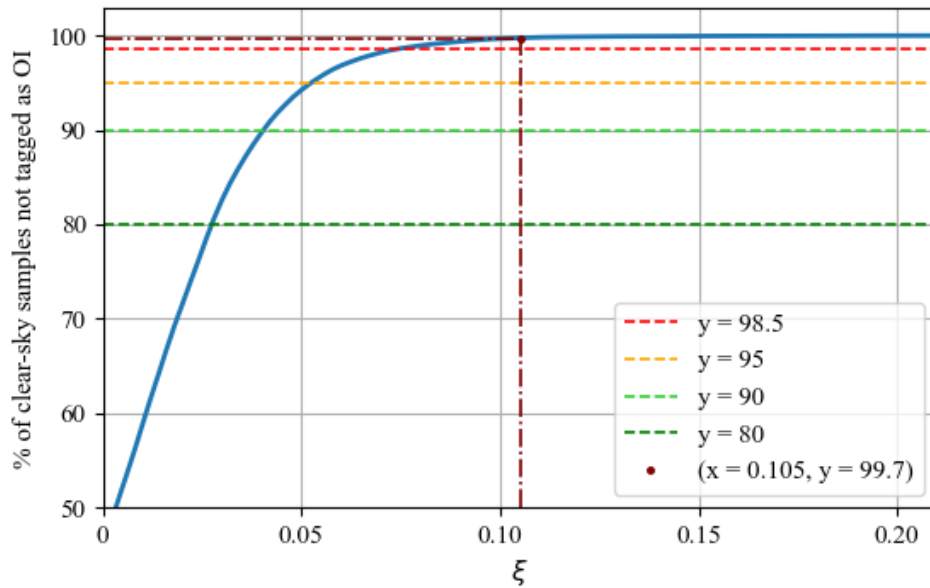
Fig. 1: Fraction (%) of clear sky samples not tagged as OI versus ξ.

This algorithm identifies 2.7 % of the OI pre-selected samples as clear-sky and these are removed, under the assumption that there is no over irradiance under clear sky conditions.

The results of the previously described OI selection algorithm are summarized in the diagram of diffuse fraction ($f_d = G_d/G$) vs. clearness index ($k_t = G/G_{toa}$, where G_{toa} is the global horizontal irradiance at the top of the atmosphere) shown in Fig. 2. This figure includes all the measurements that passed the quality control procedure as gray dots. The records identified as OI events are shown in orange and the clear sky samples are colored in light blue. Note that none of the OI samples are tagged as clear-sky.

As an example of the OI selection procedure, Fig. 3 shows the measured global (gray) and diffuse (green) together with the clear-sky estimate for one specific day, January 28 of 2020. The OI threshold is shown as a dashed brown curve and the clear-sky estimates as light blue dots. The threshold must be chosen large enough so as to avoid erroneous identification of low sun (early morning, late afternoon), clear-sky samples as OI.

2.4 Characterization of OI and OIE

An exploratory study of the selected OI's is carried out through the analysis of some of its quantifiable properties, such as intensity (irradiance value) or its frequency of occurrence. Then, we focus on the characteristics of consecutive OI events (OIE), which also have a duration (Δ, in minutes), a magnitude, *M,* defined as

$$M = \int_{t}^{t+\Delta} G\, dt \qquad\qquad\qquad\qquad (\text{eq. 2})$$

which has units of energy density (J/m^2) and a maximum or peak intensity (PI). The seasonal behavior of these characteristics is studied, as well as the occurrence distribution within a day.
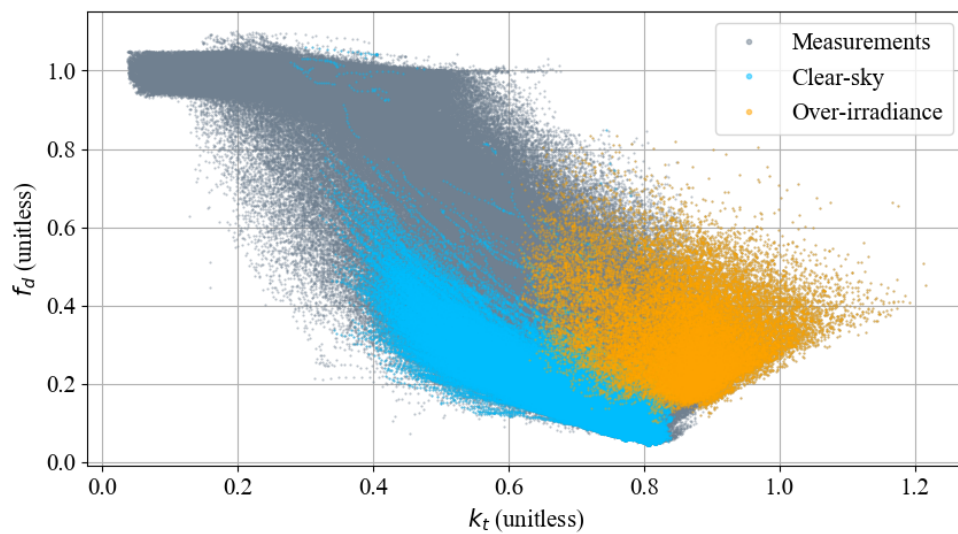
Fig. 2: Diffuse fraction (f$_d$) vs clearness index (k$_t$) diagram for the quality-checked data (shown in gray). The light blue dots indicate clear sky samples and the orange dots identify OI samples.
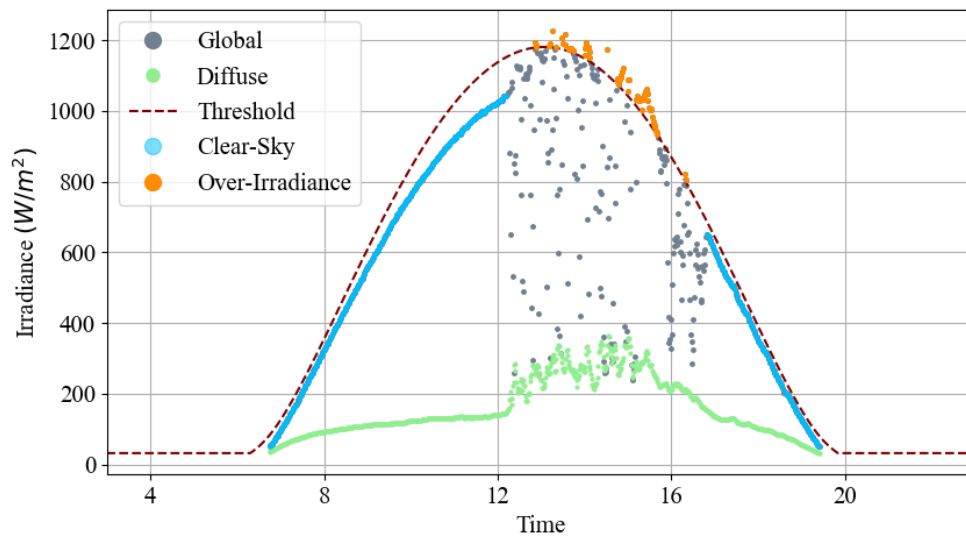
Fig.3: Example of OI detection on a time series (28/01/2020).

3. OI statistics

The OI selection procedure selects 4.2 % of the 947015 valid samples as over-irradiance. The yearly percentage of OI samples varies between 3.0 % and 4.8 % of the data in each year between 2016 and 2020, as shown in Table 3. As auxiliary information, the table presents the percentage of data which surpasses the solar horizontal irradiance at the Top Of the Atmosphere (TOA), defined as $G_{TOA} = 1361\,W/m^2 \times F_n \times cos(z)$, where z is the solar zenith angle and F_n is the orbital correction factor for day n. As expected, these samples are much rarer and are usually below 0.2 % of the total samples in each year.

Seasonal dependence is evaluated by checking the maximum values of OI registered in each season-year. For each maximum, the relative amount by which the irradiance at TOA is exceeded is indicated between parentheses. The OI subset has a maximum G of 1601 W/m² (which is 16.4 % above G_{TOA}) observed during January 2017. The maximums per year show more dispersion, ranging from 2 % to 16 % in excess of the average TOA horizontal irradiance. A similar range of values (between 1400 and 1691 W/m²) has been reported in Inman et al. (2016), De Andrade and Tiba (2016), Gueymard (2017), Castillejo-Cuberos (2020).

OIE analysis

Grouping the samples in consecutive series of OI (OIE) allows us to study the typical durations of cloud-enhancements events, as well as their magnitude in terms of accumulated energy. Figure 4 shows an histogram of the durations of OIE's. In 95% of the cases, Δ is less than 10 minutes. The behavior of Δ is quite stable between years, with small seasonal variations in the P95 duration (in minutes): 10 in summer, 12 in autumn, 8 in winter and 9 in spring.

Table 3: Characteristics of OI's by season and year.

	YEAR	2016	2017	2018	2019	2020
# of selected OI samples (%)		4.7	4.1	4.9	4.5	3.0
# of OI samples above horizontal TOA (%)		0.19	0.23	0.19	0.16	0.10
# valid data		178934	208030	173885	167910	218256
Maximum in W/m² **(% above G_{TOA}).**	**summer**	1461 (8.04 %)	1601 (16.4 %)	1435 (4.16 %)	1533 (10.8 %)	1510 (10.3 %)
	autumn	1209 (4.61 %)	1269 (11.8 %)	1225 (9.28 %)	1147 (1.83 %)	1106 (3.91 %)
	winter	1267 (14.2 %)	1239 (16.4 %)	1177 (12.9 %)	1164 (6.95 %)	1247 (16.9 %)
	spring	1557 (15.1 %)	1522 (10.8 %)	1443 (1.96 %)	1421 (2.85 %)	1433 (3.46 %)

These results, detailed by season and year, as well as the number of OIE registered can be found in Table 4. As expected, the maximum number of OIE's occurs in summer and the maximum typical duration (around 12 minutes) tends to occur in Autumn.

The magnitude (or energy density) associated with an OIE, M, is obtained from eq. (2). Seasonal histograms for M are shown in Figure 5. The figure includes the mean and the P95 magnitudes in each case. At a qualitative level, the 4 the distributions are similar. At a quantitative level, as expected, the most energetic events (both on average and in P95) occur in summer, they are moderate and similar in autumn and spring, and they are less energetic in winter. As a reference, a 5 minute OIE at constant irradiance of 1000 W/m^2 represents a magnitude of 300 kJ/m^2.
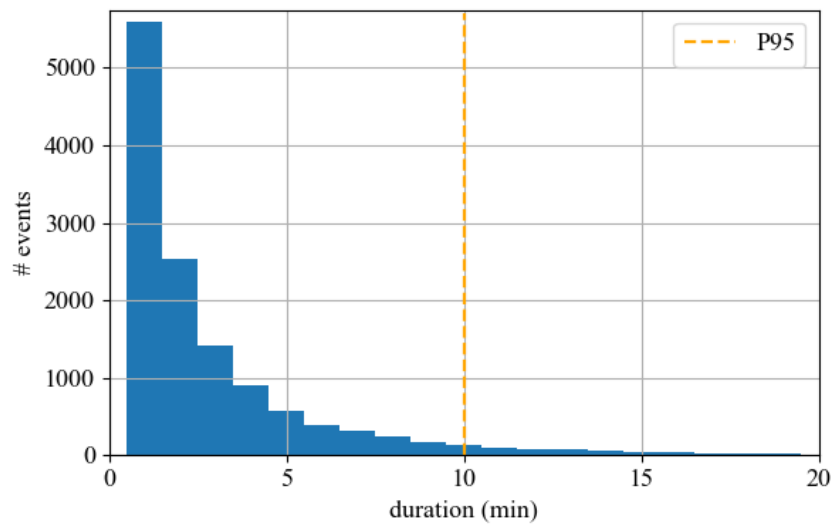
Fig 4: Histogram of Δ (min). The P95 duration is 10 minutes (vertical line).

Table 4: Number of OIE and its P95 duration by season and year. The year in which each variable records a maximum is highlighted in gray.

	YEAR	2016	2017	2018	2019	2020
Number or OIE	summer	771	1185	836	1133	800
	autumn	649	828	685	630	464
	winter	439	301	497	216	260
	spring	927	629	640	445	492
Δ at P95 (minutes)	summer	10	11	11	10	10
	autumn	12	10	13	12	11
	winter	8	7	8	9	10
	spring	9	9	9	8	10

The seasonal distribution of peak intensities (PI) of the OIEs (as well as its mean and P95 values) are shown in Figure 6. The PI distribution shows differences throughout the year. The events with the highest intensity peaks occur in both spring and summer, with mean values greater than 900 W/m² and P95 values of 1300 W/m². These values are slightly larger in spring. In autumn and winter these values are similar and decrease to approximately 660 W/m² (mean) and 1030 W/m² (P95), with slightly higher values for winter.

a. Summer, mean = 165 kJ, P95 = 521 kJ/m²   b. Autumn, mean = 126 kJ, P95 = 421 kJ/m²

c. Winter, mean = 103 kJ, P95 = 304 kJ/m²   d. Spring, mean = 139 kJ, P95 = 427 kJ/m²
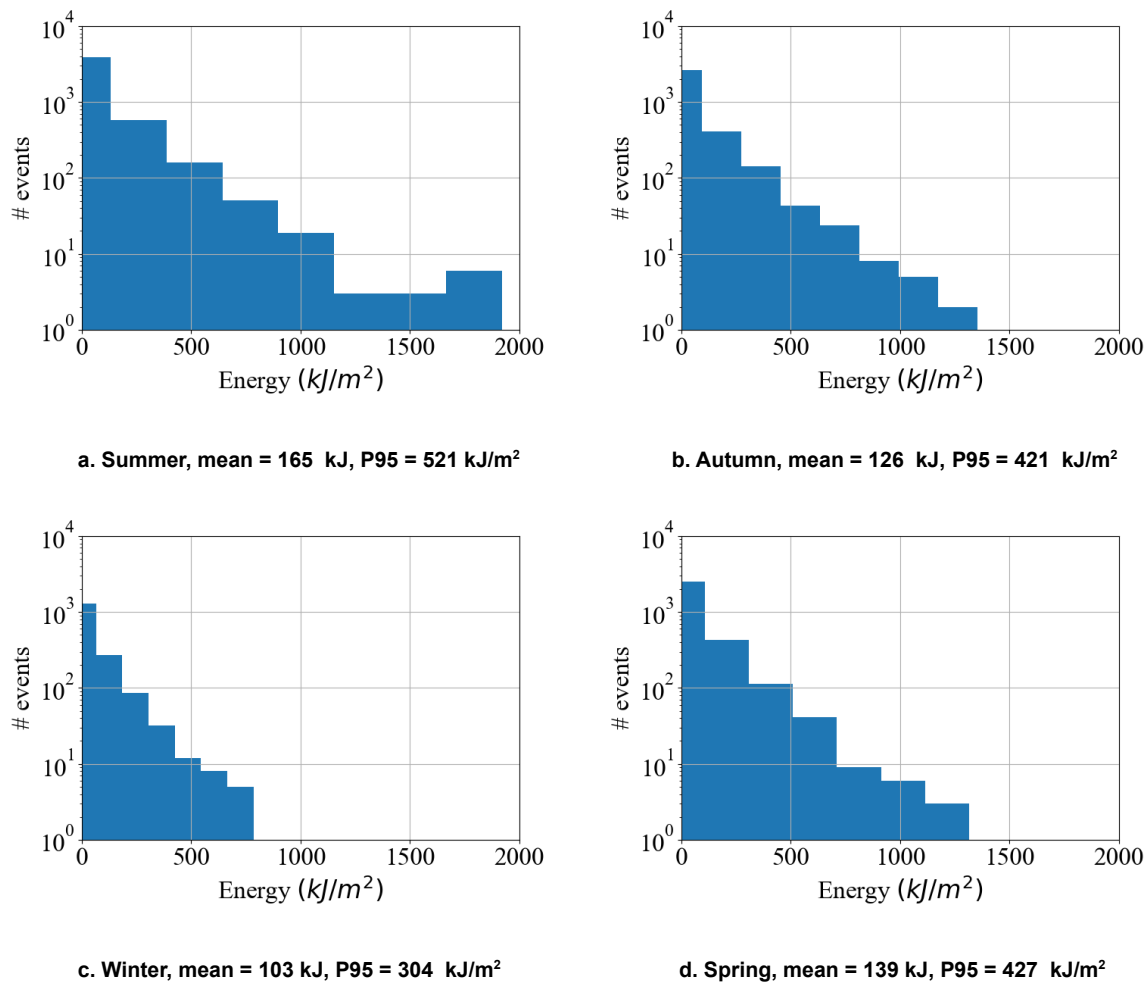
Figure 5: Histograms of Magnitude (in kJ/m2) of OIE, classified by seasons. The vertical axis is in logarithmic scale.

Finally, in addition to the seasonal dependence, we also analyze at what time of day OIE's are most likely to occur. Figure 7 shows the OIE's on a solar diagram (solar altitude vs. solar azimuth angles). Brighter colors indicate more occurences of OIE's. For winter and autumn (lower region of the diagram), the OIE's occur mainly around noon with a small trend towards the afternoon (West). In the upper region, related to spring and summer, the occurrences are more smoothly distributed with a greater presence in the regions with azimuth greater than 50º or less than -50º, that is, associated with the morning and afternoon. The behavior is almost symmetrical with a greater number of occurrences towards the afternoon.
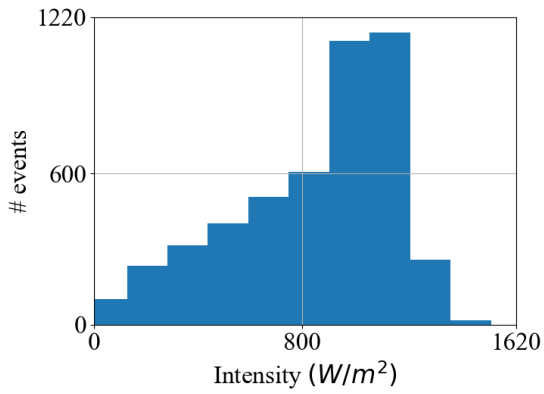
a. Summer, mean = 923 W/m², P95 = 1299 W/m²
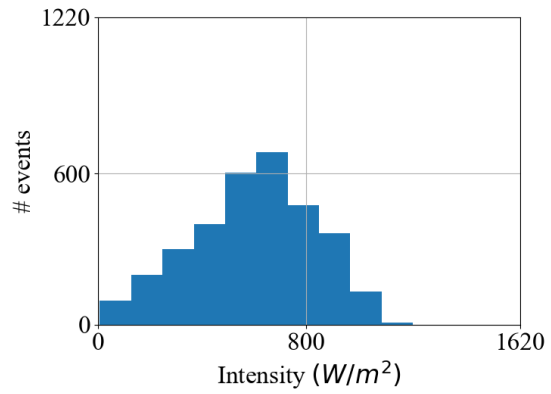
b. Autumn, mean = 658 W/m², P95 = 1022 W/m²
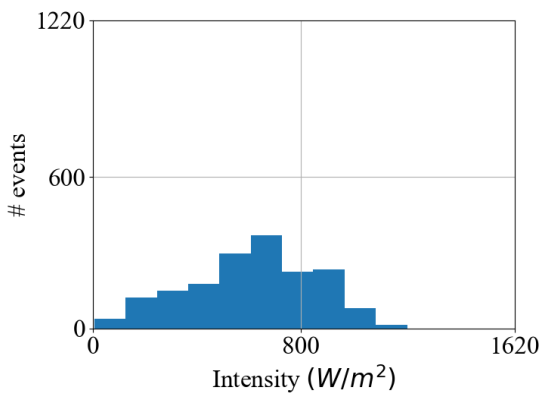
c. Winter, mean = 672 W/m², P95 = 1037 W/m²
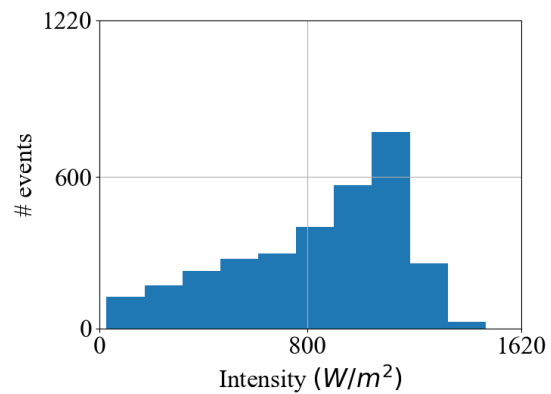
d. Spring, mean = 910 W/m², P95 = 1308 W/m²

Figure 6: Histograms of Peak Intensity (in W/m2) of OIE, classified by seasons.
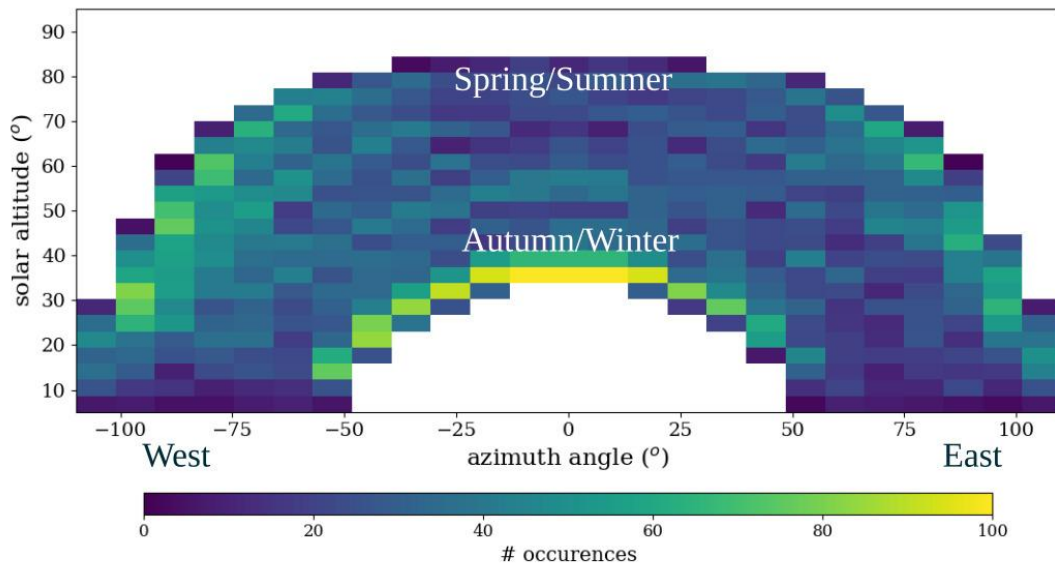
Figure 7 : Over-irradiance occurrences on a Solar diagram (solar altitude vs solar azimuth). The colors indicate the number of OIE occurrences. Azimuth is zero when looking at the equator and positive in the morning.

4. Conclusions

A first analysis of solar over-irradiance events was performed using 5 years of 1-minute data for a site in Uruguay which is representative of the broader Pampa Húmeda region. Individual samples were identified as over-irradiances (OI), based on the comparison of the GHI measurement with the clear sky estimate from an unbiased clear-sky global irradiance model. The optimal threshold factor for this method was determined. Over-irradiance events (OIE) are frequent throughout the year and represent, on average, 4.3 % of the validated data samples. The duration of these events is typically less than 10 minutes (P95), with the largest durations taking place in autumn.

The average magnitude of these events follows a clear seasonal trend: the most energetic events occur in Summer (mean of 165 kJ/m^2) and the least energetic in Winter (103 kJ/m^2), while during Autumn or Spring they have intermediate magnitudes (130 kJ/m^2). Peak intensities of OIE's are distributed according to a different pattern. The mean intensity peaks in Summer and Spring are similar (over 900 W/m^2), as are those in autumn and winter (over 650 W/m^2). However, the maximum intensity peaks (P95) are slightly greater in spring than in summer (1308 and 1299 W/m^2, respectively) and greater in winter than in autumn (1037 and 1022 W/m^2, respectively) although these differences are hardly significant. The daily distribution of OIE's has been analyzed and the OIE's in winter and autumn occur mainly around solar noon and in the early afternoon. In spring and summer, OIE's mostly occur with lower solar heights, especially in the afternoon. However, it should be noted that a 7° lower threshold has been applied to the solar data.

As future work, cloud information from sky cameras can be incorporated to correlate the selected OI samples with different types of clouds. Access to sky camera information will also allow detecting measurements with water drops at the sensor dome, which are frequent under low-sun conditions and can be incorrectly selected by the automatic algorithm as cloud enhancement. Consideration of other available variables, such as direct or diffuse irradiance, UVA and UVB measurements and pyrgeometer infrared (3 - 30 μm) sky irradiance will improve characterization of sky conditions associated to OIE's. Other clear sky models can be used for detection of OI (including satellite based ones, such as Mc Clear) in order to check the robustness of these results.

Finally, because the proposed detection method only requires GHI, its application can be generalized to other regional radiometric stations that only record that variable with 1-minute time intervals. This will allow the characterization of the spatial distribution of OIE's and their variability over a broader area.

5. References

Castillejo-Cuberos, A., Escobar, R., 2020. Detection and characterization of cloud enhancement events for solar irradiance. Solar Energy. 209, 547-567. DOI: 10.1016/j.solener.2020.09.046

De Andrade, R.,Tiba, C, 2016. Extreme global solar irradiance due to cloud enhancement in northeastern Brazil. Renewable Energy. 86, 1433-1441. DOI: 10.1016/j.renene.2015.09.01

Gueymard, C., 2017. Cloud and albedo enhancement impacts on solar irradiance using high-frequency measurements from thermopile and photodiode radiometers. Part 1: Impacts on global horizontal irradiance. Solar Energy. 153, 755-765. DOI:10.1016/J.SOLENER.2017.05.004

Gueymard, C., 2014. A review of validation methodologies and statistical performance indicators for modeled solar radiation data. Renewable and Sustainable Energy Reviews 39, pp. 1024–1034 . DOI:10.1016/j.rser.2014.07.117

Holmgren, W., C. Hansen and M. Mikofski, 2018. PVLIB Python: A Python package for modeling solar energy systems. Journal of Open Source Software 3 (29): 884. URL:htps://pvlib-python.readthedocs.io/en/stable/generated/pvlib.clearsky.detect_clearsky.html. Date accessed: 15/10/2021. DOI: 10.21105/joss.00884

Inman, R., Chu, Y., Coimbra, C.,2016. Cloud enhancement of global horizontal irradiance in California and Hawaii. Solar Energy. 130, 128-138. DOI: 10.1016/j.solener.2016.02.011

Järvelä, M., Lappalainen, K., Valkealahti, S., 2020. Characteristics of the cloud enhancement phenomenon and PV power plants. Solar Energy. 196, 137-145. DOI: 10.1016/j.solener.2019.11.090

Laguarda, A. y Abal, G., 2017. Clear-Sky broadband irradiance: first model assessment in Uruguay. En ISES Conference Proceedings, Solar World Congress 2017, Solar Radiation Availability and Variability, pp. 1–12. DOI: 10.18086/swc.2017.21.05

Laguarda, A., Giacosa, G., Alonso-Suárez, R., y Abal, G., 2020b. Performance of the site-adapted CAMS database and locally adjusted cloud index models for estimating global solar horizontal irradiation over the Pampa Húmeda region. Solar Energy, 199:295–307. DOI: 10.1016/j.solener.2020.02.005

McArthur, L., 2005. Baseline surface radiation network operations manual. Technical Report WCRP-121/ WMO TD-No. 1274, World climate research programme–WMO

Polo, J. et al., 2016. Preliminary survey on site-adaptation techniques for satellite-derived and reanalysis solar radiation datasets. Solar Energy, 132:25–37. DOI: 10.1016/j.solener.2016.03.001

Rigollier, C., Bauer, O. and Wald, L., 2000. On the clear sky model of the ESRA — European Solar Radiation Atlas — with respect to the Heliosat method. Solar Energy, 68(1):33–48. DOI: 10.1016/S0038-092X(99)00055-9

Reno, M.J. and C.W. Hansen, "Identification of periods of clear sky irradiance in time series of GHI measurements" Renewable Energy, v90, p. 520-531, 2016. DOI: 10.1016/j.renene.2015.12.031